nature research

https://doi.org/10.1038/s41567-020-01148-1

Supplementary information

Evidence for metastable photo-induced superconductivity in K_3C_{60}

In the format provided by the authors and unedited

Evidence for metastable photo-induced superconductivity in K_3C_{60}

M. Budden[1], T. Gebert[1], M. Buzzi[1], G. Jotzu[1], E. Wang[1], T. Matsuyama[1],
G. Meier[1], Y. Laplace[1], D. Pontitoli[2], M. Riccò[2], F. Schlawin[3], D. Jaksch[3], A. Cavalleri[1,3,*]

[1] *Max Planck Institute for the Structure and Dynamics of Matter, 22761 Hamburg, Germany*
[2] *Dipartimento di Scienze Matematiche, Fisiche e Informatiche, Università degli Studi di Parma, Italy*
[3] *Department of Physics, Clarendon Laboratory, University of Oxford, Oxford OX1 3PU, United Kingdom*
** e-mail: andrea.cavalleri@mpsd.mpg.de*

Supplementary Material

S1 – Sample growth and characterization

The K_3C_{60} powder pellets used in this work were prepared and characterized as previously reported in Refs. 1,2. Finely ground C_{60} powder and metallic potassium in stoichiometric amounts were placed in a vessel inside a Pyrex vial, evacuated to 10^{-6} mbar, and subsequently sealed. The two materials were heated at 523 K for 72 h and then at 623 K for 28 h. To ensure that C_{60} was exposed only to a clean potassium vapor atmosphere, solid potassium and fullerene powder were kept separated during the heating cycle. The vial was then opened under inert atmosphere (in an Ar glove box with <0.1 ppm O_2 and H_2O) and the black powder was reground, pelletized and further annealed at 623 K for 5 days. This yielded phase pure K_3C_{60} powders, as confirmed by powder X-ray diffraction measurements (Fig. S1a) that indicate an average grain size ranging from 100 nm to 400 nm. Figure S1b shows magnetic susceptibility measurements of the obtained K_3C_{60} pellets upon cooling with an external magnetic field of zero (ZFC) and 400 A/m (FC). A critical temperature around 19.8 K can be extracted, which is in agreement with literature[3].

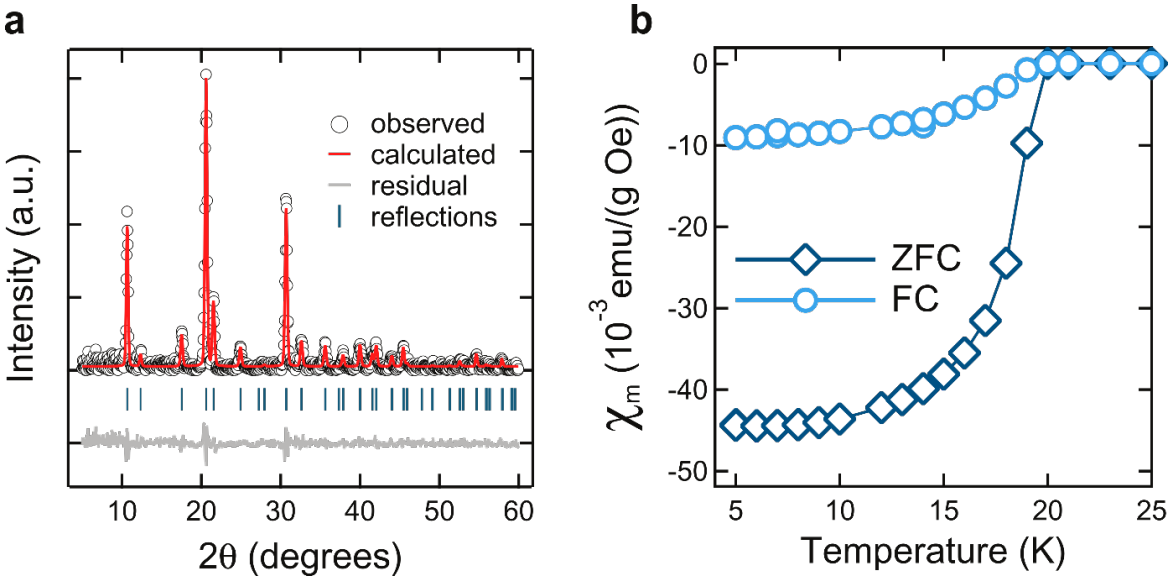

Figure S1: a. X-ray diffraction data and single f.c.c. phase Rietveld refinement for the K_3C_{60} powder used in this work. **b.** Temperature dependence of the sample magnetic susceptibility measured by SQUID magnetometry upon cooling without (ZFC: zero field cooling) and with a magnetic field applied (FC: field cooling).

S2 – Equilibrium optical properties and fitting models

The equilibrium optical properties of K_3C_{60} were retrieved in a wide spectral range from 5 meV to 500 meV at temperatures between 25 K and 300 K. For this purpose, the reflectivity of the K_3C_{60} pellet was measured by Fourier-transform infrared spectroscopy at the SISSI beamline (Elettra Synchrotron Facility, Trieste, Italy) using a commercial Fourier transform infrared spectrometer equipped with a microscope. The pellet was embedded in a sealed holder, pressed against a diamond window to obtain an optically flat interface, and attached to a helium cooled cryostat for temperature dependent measurements. To prevent degradation of the K_3C_{60} pellets, all sample handling was performed in a glove box with Argon atmosphere (<0.1 ppm O_2 and H_2O).

The K_3C_{60} reflectivity spectra were referenced against a gold mirror placed at the sample position. The low energy part of the spectrum (< 5 meV) was extrapolated using a Drude-Lorentz fitting while for the high energy side (> 500 meV) data on K_3C_{60} single crystals was used[4,5]. The complex valued optical conductivity was retrieved through a Kramers-Kronig transformation for samples in contact with a transparent window[6].

Figure S2 shows the equilibrium optical properties of K_3C_{60} at ambient pressure and at a fixed temperature T = 100 K. This and further data measured at different temperatures and pressures were already reported in Refs. 1,2 and discussed also in comparison with data obtained from single crystals.

The measured conductivity spectra were fitted by a combination of a Drude term describing the free-carrier response and a Lorentz oscillator reproducing the mid-infrared absorption at higher frequencies ($\omega_0 \sim$ 50 meV – 100 meV):

$$\sigma_1(\omega) + i\sigma_2(\omega) = \frac{\omega_p^2}{4\pi}\frac{1}{\gamma_D - i\omega} + \frac{\omega_{p,osc}^2}{4\pi}\frac{\omega}{i\left(\omega_{0,osc}^2 - \omega^2\right) + \gamma_{osc}\omega}$$

here ω_p and γ_D are the plasma frequency and scattering rate of the Drude term, while $\omega_{p,osc}$, γ_{osc}, and $\omega_{0,osc}$ are the oscillator strength, the linewidth, and the resonance frequency of the additional Lorentz term. The result of the fit is shown as a solid blue curve in Figure S2. The equilibrium data reported here were used to normalize the transient optical spectra of K_3C_{60} measured upon photoexcitation, as discussed in detail in section S4.

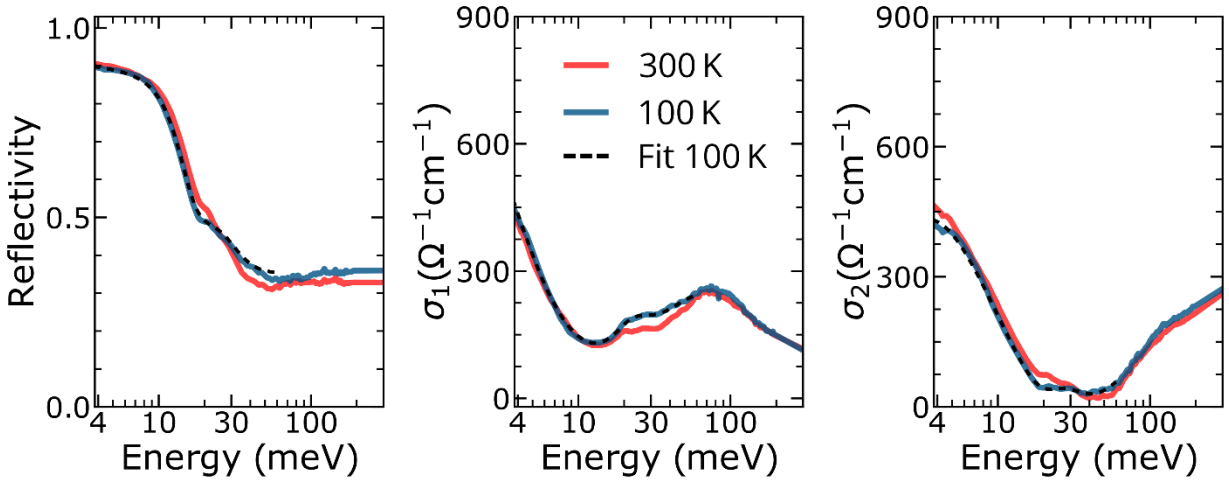

Figure S2: Equilibrium optical properties (reflectivity, real, and imaginary part of the optical conductivity) of K_3C_{60} measured at a temperature of 100 K (blue) and 300 K (red). The black dashed curve is a Drude-Lorentz fit to the optical conductivity at 100 K in the range from 3 meV to 60 meV as described in the text.

S3 – Generation of picosecond mid-infrared pump pulses

The 1 ps long pump pulses centered at 7.3 μm wavelength used for the experiments reported in Figure 2 were obtained starting from ~100 fs long, 7.3 μm wavelength pulses generated by difference frequency mixing of the signal and idler outputs of a home built optical parametric amplifier (OPA) in a 0.5 mm thick GaSe crystal. The OPA was pumped with ~60 fs long pulses from a commercial Ti:Al_2O_3 regenerative amplifier (800 nm central wavelength). To obtain a pulse duration of ~1 ps, the 7.3 μm radiation was propagated through a highly dispersive 16 mm long CaF_2 rod. The spectrum of the pump pulses was characterized using a home built FTIR spectrometer. Their duration was measured by cross-correlation with a synchronized, 35 fs long, 800 nm wavelength pulse in a 50 μm thick GaSe crystal.

This experimental setup could not efficiently produce pulses with a duration longer than few picoseconds, and also lacked the flexibility of a continuously variable pulse duration. For this reason, the experiments reported in Figure 3, 4, and 5, were obtained with a new optical device based on CO_2 lasers that generated longer, narrow-band pulses centered at 10.6 μm wavelength, with fully tunable duration between 5 ps and 1.3 ns.

To perform mid-infrared pump, THz probe experiments, the pump pulses generated from the CO_2 laser system needed to be synchronized to the Ti:Al_2O_3 laser generating the THz probe light (see section S4). To achieve this, we developed the setup described in Figure 3a.

Here, ~150 fs long, 10.6 μm wavelength pulses were generated by difference frequency mixing of the signal and idler outputs of a home built OPA in a 1.5 mm thick GaSe crystal. The OPA was pumped with ~100 fs long pulses from a commercial Ti:Al_2O_3 regenerative amplifier (800 nm wavelength). A fraction of these femtosecond pulses (~60 pJ) were injected through the semitransparent front window (20 % transmission) into the cavity of a commercial transversely excited atmosphere (TEA) CO_2 laser. The injection of 10.6 μm wavelength seed pulses, induces a temporal mode locking resulting in a train of output pulses, which are synchronized to the femtosecond seed laser[7]. Because of the high finesse of the CO_2 laser oscillator cavity, the seed pulses were spectrally filtered and the oscillator produced pulses with nanosecond duration. The most intense pulse from the train was selected with a custom designed CdTe Pockels cell and mid-infrared wire grid polarizers. The resulting output consisted of a single pulse with a duration of ~1.3 ns and a pulse energy of ~730 μJ per pulse at 18 Hz repetition rate. This pulse was then amplified further in a second ten-pass amplifier based on a modified commercial TEA CO_2 laser. The typical pulse energy achieved after the amplifier is ~11 mJ at 18 Hz repetition rate, with a pulse duration of ~1.3 ns.

The pulse duration of these 1.3 ns long pulses, was tuned using a combination of a plasma-mirror and -shutter, which allows "slicing" of the leading and trailing edge of the mid-infrared (MIR) pulses. For both plasma slicers we utilized semiconductor wafers transparent to the 10.6 μm radiation (Si, Ge, or CdTe) set at the Brewster's angle to suppress the reflection of the p-polarized MIR beam. A pair of time-delayed, intense femtosecond pulses (λ = 800 nm, 100 fs duration) was used to photoexcite the semiconductors to create an electron hole plasma at the surface that acts as an ultra-fast switchable mirror[8-10]. Varying the time delay between the two femtosecond pulses enabled us to tune their pulse duration between 5 ps and 1.3 ns. To compensate the path length in the cavities of the CO_2 laser and amplifier (~300 m), the slicing pulses were derived from a second Ti:Al_2O_3 amplifier. This was optically synchronized to the one used for generating the seed pulses for the CO_2 laser by seeding it with pulses from the same Ti:Al_2O_3 master oscillator.

The envelope of the sliced mid-infrared pulses is affected by the decay time of the electron/hole plasma in the semiconductor. When using n-doped silicon, the long carrier recombination time yielded pulses that have an almost flat-top shape for different pulse lengths up to ~300 ps. The pulse envelope of the generated pulses was measured by cross-

correlation with a synchronized 100 fs long, 800 nm wavelength pulse in a 2 mm thick GaSe crystal (Figure S3).

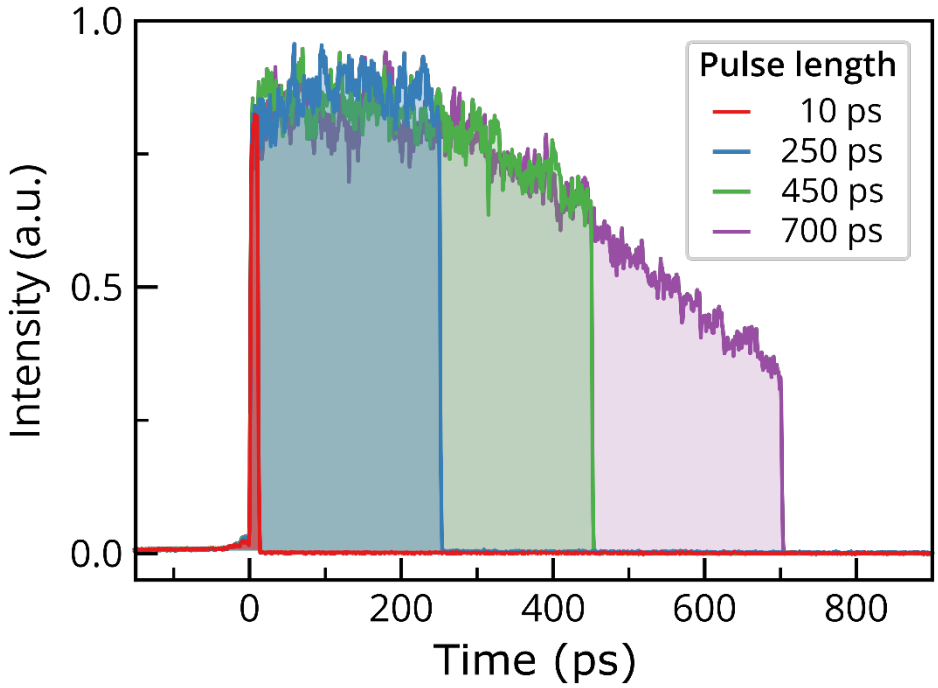

Figure S3: Time profile of the 10.6 μm pulses generated by slicing in two photo-irradiated n-doped silicon wafers. These traces are a result of a cross-correlation measurement following the procedure described in the text.

S4 – Determination of the out-of-equilibrium optical response

The mid-infrared pump-THz probe experiments presented in Figures 1, 2, and 3 were performed on compacted K_3C_{60} powder pellets pressed against a diamond window to ensure an optically flat interface. As K_3C_{60} is water and oxygen sensitive, the pellets were sealed in an air-tight holder and all sample handling operations were performed in an Argon filled glove box with <0.1 ppm O_2 and H_2O. The sample holder was then installed at the end of a commercial Helium cold-finger (base temperature 5 K), to cool the pellets down to a temperature of 100 K. Although a detailed study of the sample damage threshold was not carried out, no damage was observed up to 4.5 mJ/cm^2 for 100 fs pulses and up to fluences in excess of 50 mJ/cm^2 for pulses longer than 1 ps.

The mid-infrared pump induced changes in the low frequency optical properties, were retrieved using transient THz time domain spectroscopy in two different experimental setups. The THz pulses were generated in a commercial photoconductive emitter or in a 0.2 mm thick

(110)-cut GaP crystal using 800 nm pulses with a duration of 100 fs and 35 fs, respectively. In both cases, these 800 nm pulses were generated by the Ti:Al_2O_3 laser optically synchronized with the one producing the mid-infrared excitation pulses. The generated probe pulses were focused at normal incidence on the K_3C_{60} sample, and their electric field profile was measured, after reflection from the sample, by electro-optic sampling in 1 mm thick ZnTe, or 0.2 mm thick GaP (110)-cut crystals. The ZnTe based setup had a measurement bandwidth ranging from 3.3 meV to 12 meV, while the GaP based one spanned the range between 4.1 meV to 29 meV. The time resolution of both setups is determined by the measurement bandwidth and is ~300 fs and ~150 fs, respectively.

To minimize the effects on the pump-probe time resolution due to the finite duration of the THz probe pulse, we performed the experiment as described in Refs. 11,12. The transient reflected THz field at each time delay τ after excitation was obtained by fixing the delay τ between the pump pulse and the electro-optic sampling gate pulse, while scanning the delay t of the single-cycle THz probe pulse.

The electric field reflected by the unperturbed sample, $E_R(t)$, and the pump-induced changes, $\Delta E_R(t,\tau)$ were simultaneously acquired at each time delay τ by acquiring the electro-optic sampling signals and chopping the pump and probe beams at different frequencies. Simultaneous measurement of the reference electric field $E_R(t)$ and the light-induced changes $\Delta E_R(t,\tau)$ avoids the introduction of possible phase artifacts (e.g. due to long term drifts) and is particularly useful when the measured electric field contains fast-varying frequencies. $E_R(t)$ and $\Delta E_R(t,\tau)$ were then independently Fourier transformed to obtain the complex-valued, frequency dependent $\tilde{E}_R(\omega)$ and $\Delta\tilde{E}_R(\omega,\tau)$. The photo-excited complex reflection coefficient $\tilde{\mathrm{r}}(\omega,\tau)$ was determined by

$$\frac{\Delta\tilde{E}_R(\omega,\tau)}{\tilde{E}_R(\omega)} = \frac{\tilde{\mathrm{r}}(\omega,\tau) - \tilde{\mathrm{r}}_0(\omega)}{\tilde{\mathrm{r}}_0(\omega)},$$

where $\tilde{\mathrm{r}}_0(\omega)$ is the stationary reflection coefficient known from the equilibrium optical response (see Supplementary Section S2).

As the mid-infrared pump penetrated less ($d_{pump} \approx 0.2$ μm) than the THz probe ($d_{probe} \approx 0.6 - 0.9$ μm), these light-induced changes, measured at each pump-probe delay τ, were reprocessed to take this mismatch into account. As the pump penetrates in the material, its intensity is reduced and it induces progressively weaker changes in the refractive index of the

sample. A sketch of this scenario is shown in Figure S4, which was modelled by considering the probed depth of the material d_{probe} as a stack of thin layers, with a homogeneous refractive index and assuming the excitation profile to follow an exponential decay. By calculating the complex reflection coefficient of this "multilayer" system with a characteristic matrix approach[13], the complex refractive index at the surface $\tilde{n}(\omega,\tau)$, can be self-consistently retrieved. From this, the complex conductivity for a homogeneously transformed volume was obtained as:

$$\sigma(\omega,\tau) = \frac{\omega}{4\pi i}[\tilde{n}(\omega,\tau)^2 - 1].$$

The only free parameter in this modelling is the intensity penetration depth of the mid-infrared pump, which is determined by the equilibrium intensity extinction coefficient at the pump wavelength, $\lambda_{pump}/4\pi Im(\tilde{n}_0(\omega = \omega_{pump}))$. The probe penetration depth d_{probe} is a frequency- and time-dependent quantity that was self-consistently extracted from the transient response of the material $Im(\tilde{n}(\omega,\tau))$ through the multilayer modelling.

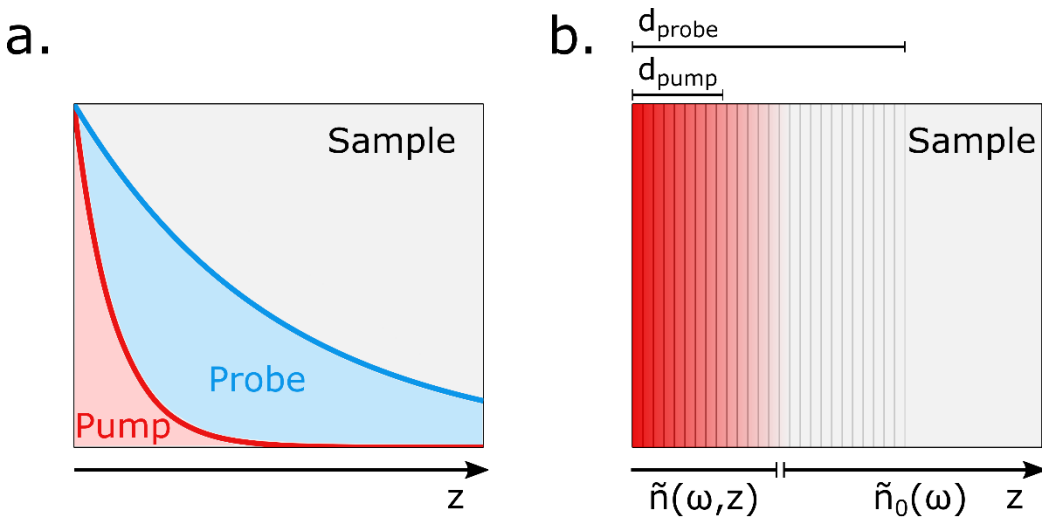

Figure S4: a Schematics of pump-probe penetration depth mismatch. **b** Multi-layer model with exponential decay used to calculate the pump-induced changes in the complex refractive index $\tilde{n}(\omega,\tau)$ for each pump-probe delay τ. The transition from red to background (grey) represents the decaying pump-induced changes in $\tilde{n}(\omega,z)$.

S5 – Influence of uncertainties in the equilibrium optical properties

The error of the reconstructed light induced transient optical response of K_3C_{60} is primarily determined by uncertainties in: (i) the measured values of the normalized change of the electric field $\Delta E/E$, (ii) the pump penetration depth d_{pump}, which is used to reconstruct the $\tilde{n}(\omega, z)$ profile in the multilayer model (see Supplementary Section S4), and (iii) the absolute

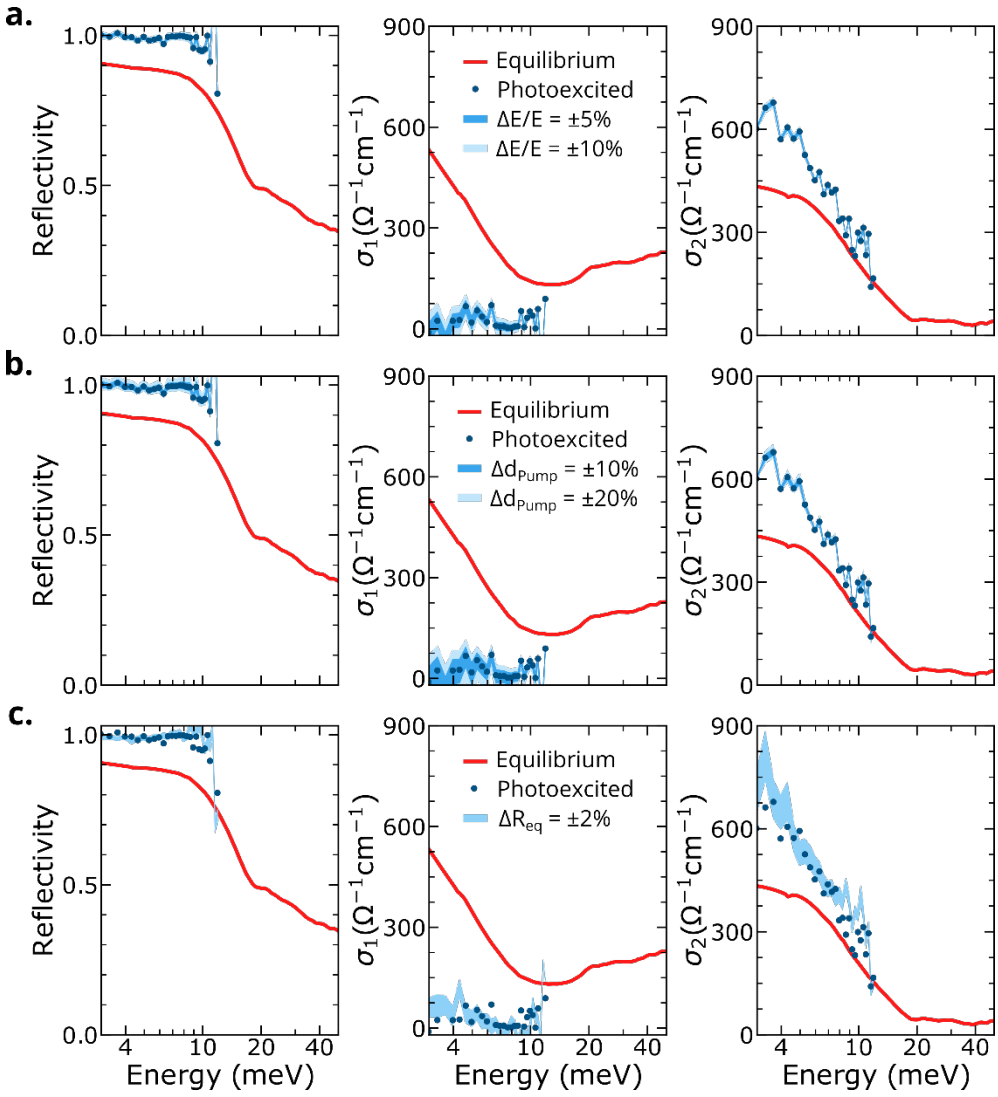

Figure S5: Errors in the obtained transient optical properties caused by different possible sources of uncertainty. The propagated error on the optical properties is shown as light and dark blue coloured bands and was propagated from **a.** ±5% and ±10% uncertainty in the measured $\Delta E/E$, **b.** ±10% and ±20% uncertainty in the value of the pump penetration depth and **c.** ±2% uncertainty in the value of the equilibrium R(ω). All measurements (red curves at equilibrium and blue dots 1 ns after photoexcitation) were carried out at T = 100 K. Photoexcitation was performed in the same conditions as the data presented in figure 3 of the main text.

value of the measured equilibrium reflectivity, which is typically smaller than 2%. To display the effect of these uncertainties we display transient optical properties reconstructed from the $\Delta E/E$ values measured 1 ns after photo-excitation at a temperature T=100 K.

In Figure S5a, S5b, and S5c we show as shaded colored bands the propagated uncertainties introduced by $\pm 5\%$ and $\pm 10\%$ variations in $\Delta E/E$, $\pm 10\%$ and $\pm 20\%$ uncertainties in the value of d_{pump}, and a $\pm 2\%$ error in the value of the equilibrium reflectivity $R(\omega)$ respectively. Importantly, all features of the light induced response such as the gap opening in $\sigma_1(\omega)$ and the presence of a divergence in $\sigma_2(\omega)$ are not affected by any of these uncertainties.

S6 – Drude-Lorentz fits of the out-of-equilibrium optical response

The out-of-equilibrium optical response of the photo-irradiated K_3C_{60} pellets was modelled by fitting simultaneously the reflectivity and complex optical conductivity with the same Drude-Lorentz model used to fit the equilibrium response described in Section S2:

$$\sigma_1(\omega) + i\sigma_2(\omega) = \frac{\omega_p^2}{4\pi}\frac{1}{\gamma_D - i\omega} + \frac{\omega_{p,osc}^2}{4\pi}\frac{\omega}{i\left(\omega_{0,osc}^2 - \omega^2\right) + \gamma_{osc}\omega}$$

As previously reported[1], this model is also able to capture the photo-induced superconducting-like response of K_3C_{60} as in the limit of $\gamma_D \to 0$ the Drude conductivity can capture the response of a superconductor below gap:

$$\sigma_1(\omega) + i\sigma_2(\omega) = \frac{\pi}{2}\frac{N_S e^2}{m}\delta[\omega = 0] + i\frac{N_S e^2}{m}\frac{1}{\omega} + \frac{\omega_{p,osc}^2}{4\pi}\frac{\omega}{i\left(\omega_{0,osc}^2 - \omega^2\right) + \gamma_{osc}\omega}$$

Here N_S, e, and m are the superfluid density, electron charge, and mass, respectively. Furthermore, the transient nature of a photo-induced superconductor having a finite lifetime appears as a broadening of the zero-frequency Dirac delta[14].

The data acquired with broadband THz probe (Figure 2) were fitted by optimizing iteratively the parameters of both the Drude (ω_p and γ_d) and mid-infrared absorption band ($\omega_{p,osc}$, $\omega_{0,osc}$, and γ_{osc}). On the other hand, data acquired with narrower probe bandwidths (Figure 3) were fitted also by keeping only ω_p and γ_d free to vary. Importantly, in both cases the fits

yielded similar Drude parameters and we chose to only optimize the Drude parameters for these data as the probed frequency range does not overlap with the mid-infrared oscillator. Figure S6 shows representative fits to data measured at 100 K for three different time delays of -150 ps, -100 ps, and 10 ps. The fitting was performed on transient conductivity spectra for each time delay shown in Figure 4a. The obtained parameters were used to calculate the zero-frequency extrapolated optical conductivity σ_0 and from this the "optical resistivity" ρ_0 as:

$$\rho_0 = {}^1/_{\sigma_0} = \lim_{\omega \to 0} {}^1/_{\sigma_1(\omega)}$$

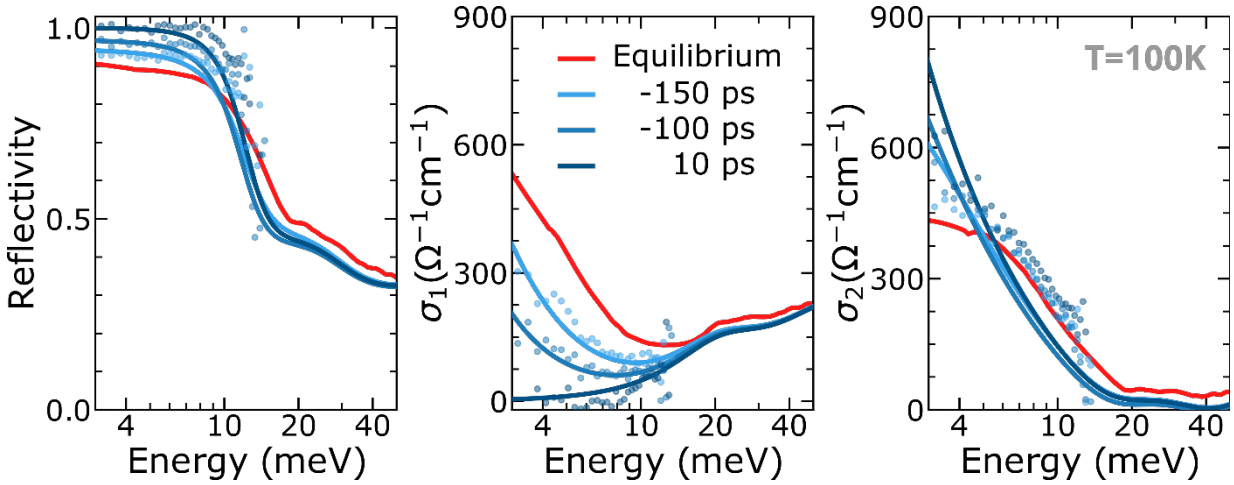

Figure S6: Measured optical properties (reflectivity, real, and imaginary part of the optical conductivity) of K_3C_{60} measured at a temperature of 100 K at equilibrium (red curve) and at three different time delays of -150 ps, -100 ps, 10 ps (blue filled symbols). These data were acquired with a pump-pulse duration of 200 ps and by definition the time delay is zero when the pulse ends (cf. Figure 3c). The solid lines are Drude-Lorentz fits to the transient optical properties.

S7 – Sample preparation for electrical transport measurements

For time-resolved electrical transport measurements, pellets of K_3C_{60} were integrated into a sample carrier with patterned microstrip transmission lines. Fig. S7 shows a picture of the sample carrier and a sketch of its cross-section. The four Ti (10 nm)/Au (270 nm) microstrip structures were grown using a combination of e-beam evaporation, laser-lithography, and lift-off processing, on a 500 µm thick diamond substrate, transparent to the 10.6 µm radiation. The wave impedance of the transmission lines was adapted to 50 Ω. A pellet of 1 mm diameter and ~75 µm thickness was made from K_3C_{60} powders with a pellet die and a manual press. All the sample handling operations were carried out in an Argon filled glove box with <0.1 ppm

O_2 and H_2O to prevent sample oxidation. To ensure good electrical contact between the polycrystalline pellet and the transmission lines at low temperatures, a layer of 2 µm thick Indium was deposited on the inner parts of the Au transmission lines by an additional lithography and lift-off step. To reproducibly position the pellet in the center of the four microstrips, a ~50 µm thick layer of photoresist (SU8) with a 1 mm central bore was deposited. The K_3C_{60} pellet enclosed in the photoresist layer, was then capped with a 500 µm thick sapphire plate and sealed with vacuum compatible glue. This assembly was placed on a copper holder and then installed at the end of a commercial LHe cold-finger, in order to cool the K_3C_{60} pellets down to a base temperature of 5 K. The microstrips were terminated to SMP connectors to connect them to 50 Ω wave impedance coaxial cables that are thermally anchored on the cold finger, and routed to the outside of the cryostat.

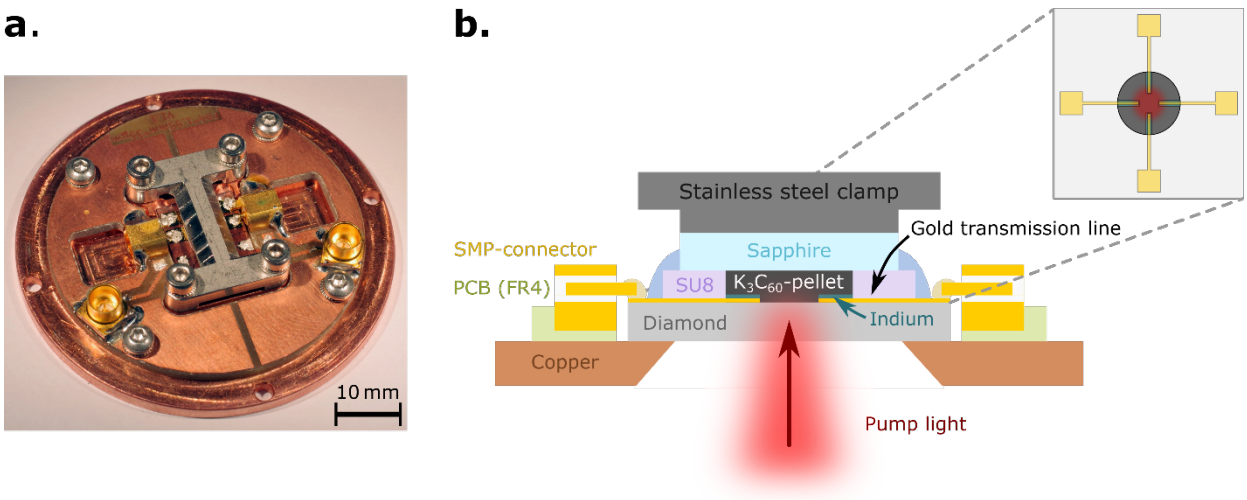

Figure S7: a. Photograph of the sample carrier used for transport measurements. **b.** Schematic section-view of the K_3C_{60} sample assembly (not to scale). The pulsed mid-infrared excitation reaches the sample from below. The upper right panel shows a sketch of the electrode geometry similar to the one used in both four- and two-terminal measurements.

S8 – Time-resolved electrical transport measurements

Standard four-terminal resistance measurements (Figure S8a) were performed on K_3C_{60} pellets encapsulated in the high-frequency sample carrier using a lock-in technique with a sinusoidal excitation current of amplitude $I_{source} = 1$ µA at a frequency of 300 Hz. While this technique provides accurate values of the low frequency sample resistance R_{sample} it could only be applied up to frequencies of a few MHz due to the limited bandwidth of the high input impedance differential amplifiers as well as parasitic capacitances in the circuit.

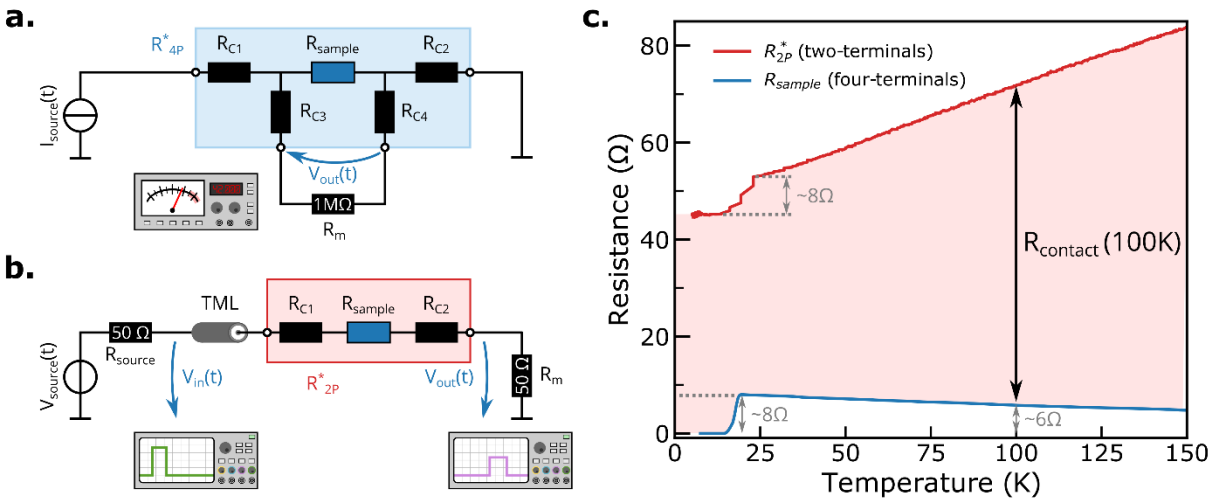

Figure S8: a. Equivalent circuit of a four-terminal resistance measurement. A constant amplitude sinusoidal current is injected into R_{sample} through the contact resistances R_{C1}, and R_{C2}. The voltage drop across R_{sample} is detected by a high input impedance lock-in amplifier through the contact resistances R_{C3} and R_{C4}. The sample resistance can be directly retrieved as V_{out}/I_{source}. **b.** Equivalent circuit for two-terminal measurements. The sample with intrinsic resistance R_{sample} and contact resistances R_{C1} and R_{C2} is connected via two terminals. TML indicates the coaxial cable which acts as a transmission line for high frequency signals. **c.** Temperature dependent resistance measured in a two- and four-terminal measurement. The temperature-dependent contact resistance $R_{contact} = R_{C1} + R_{C2}$ is displayed as red shading inbetween the graphs. Both measurements were performed on the same type of pellet with identical preparation procedure and equal electrode geometry.

The lifetime of the light-induced superconducting state is several nanoseconds, hence four-terminal measurements are too slow to probe transport properties on these time scales. To overcome this issue, we performed high-frequency two-terminal resistance measurements. These measurements were conducted by launching a 1 ns long voltage pulse from a commercial pulse generator through the microstrip transmission lines and the K_3C_{60} pellet in the sample carrier. A gated integrator was then used to detect the amplitudes of the injected voltage pulse $V_{in}(t)$, and of the one transmitted through the sample $V_{out}(t)$. An equivalent circuit diagram of this two-terminal measurement is shown in Figure S8b.

These measurements allow to retrieve the resistance $R^*_{2P} = R_{sample} + R_{C1} + R_{C2}$ which includes contributions from wiring and contact resistances. As the injected voltage pulse propagates, it can be reflected at the input and output terminals of R^*_{2P} due to a possible impedance mismatch. To account for this, it is convenient to describe the propagation of the pulse through the network using the two-port scattering matrix formalism[15], from which the total resistance of the sample R^*_{2P} can be retrieved as:

$$R_{2P}^{*} = R_{sample} + R_{C1} + R_{C2} = 2\left(\frac{V_{in}}{V_{out}} - 1\right) R_m.$$

Here, V_{in} and V_{out} are the amplitudes of the injected pulse and of the pulse transmitted through the sample while R_m = 50 Ω is the input impedance of the gated integrator used for signal detection. This result was quantitatively verified by simulating the equivalent circuit with the software QucsStudio starting from measured values of the elements in the circuits (see Supplementary Material S9 for more details).

Extracting R_{sample} from R_{2P}^{*} requires knowledge of the contact resistance from the low-frequency four-terminal measurements. In order to calibrate the contact resistance $R_C = R_{C1} + R_{C2}$ we compared the temperature dependence of the resistance R_{2P}^{*} (measured in the pulsed two-terminal geometry, red curve in Fig. S8c) to that of the sample resistance R_{sample} (measured in the four-terminal geometry, blue curve in Fig. S8c). In both measurements, the equilibrium superconducting transition of K_3C_{60} is observed as a drop in the measured resistance of ~8 Ω as the sample becomes superconducting. Hence, the two- and four-terminal measurements are equally sensitive to changes in R_{sample} and are only offset by the contact resistance R_C (red shaded area in Figure S8c), allowing us to extract R_{sample} from the high-frequency two-terminal measurements.

The time-resolved resistance measurements of the photo-irradiated K_3C_{60} pellet shown in Figure 4b were performed at 100 K by repeating the pulsed two-terminal measurements at different time delays after photoexcitation. This was achieved by electronically synchronizing the pulse generator that provided the probe voltage pulse to the laser system. These measurements yielded the total resistance R_{2P}^{*}, from which the contact resistance $R_C(100\ \mathrm{K}) = 66\ \Omega$ was subtracted to obtain the time-dependent resistance of the K_3C_{60} sample alone. Note that the change of the resistance in the time-resolved experiment at T = 100 K is ΔR = 6 Ω (Figure 4), which is what is quantitatively expected from the DC four-terminal measurement if the sample turns superconducting at this temperature.

S9 – Modeling time-resolved electrical transport measurements

To ensure that the experimental procedure used to extract the sample resistance (described in Supplementary Section S8) was not affected by additional contribution due to stray

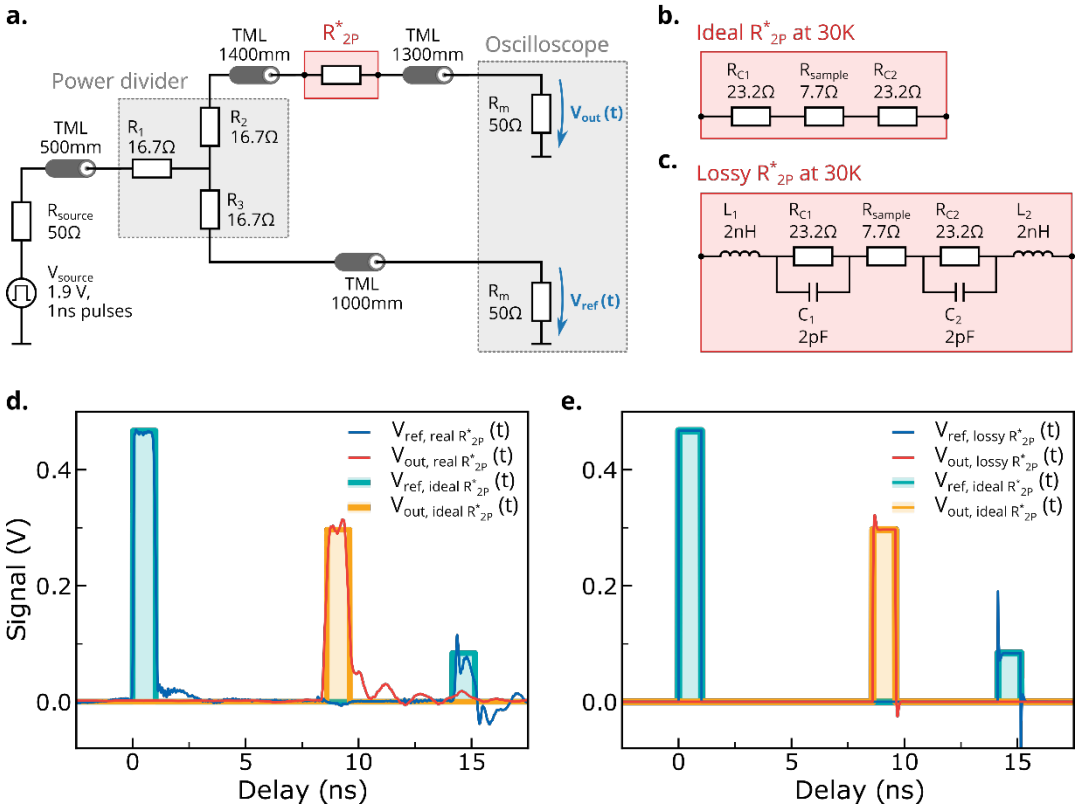

Figure S9: a. Schematic description of the setup for measuring the unknown R^*_{2P} resistance in a two-terminals configuration. TML denotes HF compatible microstrip transmission lines. Their length was adjusted so that pulses are not overlapping when measured on the oscilloscope. **b.** Ideal equivalent circuit diagram for R^*_{2P} consisting of two contact resistors ($R_{C1}$and R_{C2}) and the intrinsic resistance of the sample (R_{Sample}). **c.** Lossy equivalent circuit diagram for R^*_{2P} considering a capacitive as well as inductive component of the contacts. **d.** Time traces for $V_{ref}(t)$ (blue) and $V_{out}(t)$ (red) measured at a temperature of 30K without photo-excitation and corresponding numerical simulations (green and yellow lines) performed under the assumption of an ideal R^*_{2P}. The measured oscillations at the base of the first pulse in $V_{out}(t)$ and the second pulse in $V_{ref}(t)$ are caused by residual reflections not relevant to our analysis. **e.** Comparison of two simulations with ideal and lossy R^*_{2P}. Parasitic capacitances and inductances of 2 pF and 2 nH were introduced resulting in voltages spikes that are bigger than any deviation observed between the measurement and the ideal case simulation.

impedances we have modelled the experimental setup using the software QucsStudio, that simulates propagation of electrical signals in the time domain.

The simulations were performed according to the setup described in Figure S9a, that matches closely the experimental setup. A 1ns long voltage pulse generated by a commercial pulse generator, was split in two identical replicas by a power divider; one was sent through the sample while the other was used as a reference. Both pulses were sampled with a real-time oscilloscope with 20 GHz bandwidth and 80 GSamples/s. The recorded signals are referred to as $V_{out}(t)$ and $V_{ref}(t)$ in the following.

Figure S9d shows the $V_{out}(t)$ and $V_{ref}(t)$ time traces (red and blue lines) measured at 30 K, and corresponding simulations (green and yellow lines) of the equivalent circuit diagram shown in figure S9a, where the two-terminal resistance R_{2P}^{*} is simply modelled by two contact resistors ($\mathrm{R_{C1}}$ and $\mathrm{R_{C2}}$) and the intrinsic sample resistance (R_{sample}). Remarkably, all peak positions and amplitudes are reproduced with good agreement. The $V_{ref}(t)$ trace, shows the injected pulse at ~0 ns and a later pulse, around ~13.5 ns which is a reflection from the sample arm. The $V_{out}(t)$ trace shows a pulse appearing at ~8 ns which is the injected pulse after propagation through the sample and contacts. Because of the voltage drop across R_{2P}^{*} it has lower amplitude compared to the injected pulse.

As mentioned in Supplementary Section S8, the propagation of voltage pulses through this network can be described by applying the two-port scattering matrix formalism to retrieve the sample resistance R_{sample} directly from the amplitude of the reference (V_{in}) and transmitted (V_{out}) pulses as:

$$R_{2P}^{*} = R_{sample} + R_{C1} + R_{C2} = 2\left(\frac{V_{in}}{V_{out}} - 1\right) R_m$$

where R_m is the internal impedance of the oscilloscope, R_{C1}, and R_{C2} are the contact resistances. For an accurate measurement of R_{2P}^{*} it is important that the amplitude of the reference and transmitted pulses is not changed by parasitic effects.

To evaluate the influence of possible parasitic capacitances at the contacts, that might short the contact resistance at high frequencies, we simulated the extended equivalent circuit diagram for R_{2P}^{*} shown in Supplementary Figure S8c. We estimated 2 pF and 2 nH as realistic upper limits for the respective capacitance and inductance values. The results of these simulations are compared to those in the ideal case in Supplementary Figure S9e. The additional stray impedances resulted in voltage spikes on top of the nanosecond pulses, that are stronger in amplitude than the deviations observed between the measured signals and simulations in the ideal case. A similar simulation (not shown) with additional parasitic capacitances to ground yielded comparable results, the only differences were due to the lower bandwidth of the circuit.

The good agreement between the ideal simulations and our measured signals strongly suggests that capacitive and inductive contributions to the contact resistance are negligible. More importantly, these putative contributions do not lead to a significant change of the average pulse amplitude which is used to calculate the resistance.

S10 – Pulse length dependence of the out-of-equilibrium metastable state

In analogy to Figure 5, Figure S10 shows excitation-pulse length dependent data extracted from transient THz time domain spectroscopy measurements. Here, we plot the reduction of spectral weight in the real part of the optical conductivity (lower panels) as

$$\Delta\sigma_1 = \int_{2.2meV/\hbar}^{10meV/\hbar} \sigma_1^{trans}(\omega) - \sigma_1^{eq}(\omega)\, d\omega,$$

upon excitation with mid-infrared pulses of different duration varying between 250 ps and 700 ps (top panels). The excitation fluence was kept constant to a value of 22 mJ/cm^2. The data indicates that $\Delta\sigma_1$ measured 100 ps and 500 ps after excitation is independent of the excitation pulse duration. This is in agreement with the pulse-length dependent data presented in Fig. 5 and measured by electronic transport. Pump pulse lengths shorter than 250 ps were not measured here since the fluence of 22 mJ/cm^2 could not be achieved for these shorter pulses.

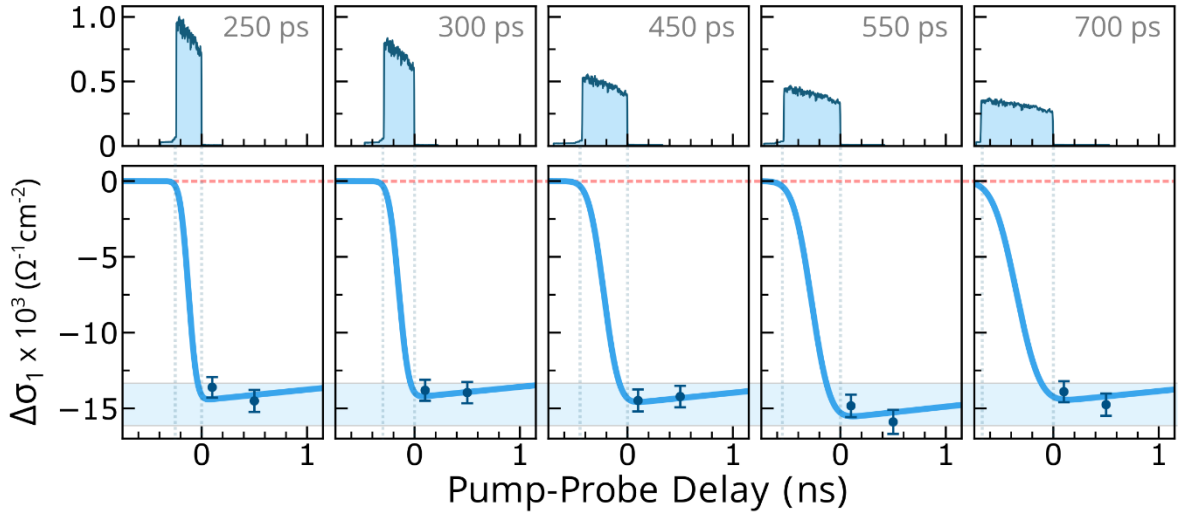

Figure S10.1: (lower panels) Pump pulse length dependence of the spectral weight loss $\Delta\sigma_1$ (as defined in the text) induced upon photoexcitation and measured at time delays of 100 ps and 500 ps for different pump pulse durations. The red dashed line displays the equilibrium value of $\Delta\sigma_1$. **(upper panels)** Excitation pump pulse profiles of the mid infrared pulses measured via cross-correlation (see Section S3). The blue curves are a guide to the eye indicating the typical time dependence of the signal. All measurements were performed at a constant fluence of 22 mJ/cm^2, excitation wavelength of 10.6 µm, and base temperature T = 100 K.

We have also measured the dependence of the time resolved optical properties on the pulse length at constant peak electric field of the excitation pulse. Figure S10.2 shows the time dependence of the real part of the optical conductivity $\langle\sigma_1\rangle$, averaged in the 2-10meV range, for excitation pulse lengths between 10 ps to 75 ps. This quantity displays the degree of gapping of $\sigma_1(\omega)$ and is used as a metric for light-induced superconductivity. For short pulses and low fluences (Fig. S10.2 a,b) we observe that $\langle\sigma_1\rangle$ approaches zero - indicating full gapping - only during the drive, similarly to what shown in Fig. 1d. A few picoseconds after the drive terminates, $\langle\sigma_1\rangle$ relaxes to a metastable value with only partial gapping. The decay time of this intermediate, partially gapped state is ≈10 ns. As the fluence is increased, the value of $\langle\sigma_1\rangle$ in the metastable state eventually approaches zero, indicating full gapping (Fig. S10.2 d).

Instead of increasing the lifetime of the short-lived state, higher fluences lead to the appearance of a distinct, metastable state with a decay time which is independent of the fluence and excitation pulse duration (see shaded areas in Fig. S10.2).

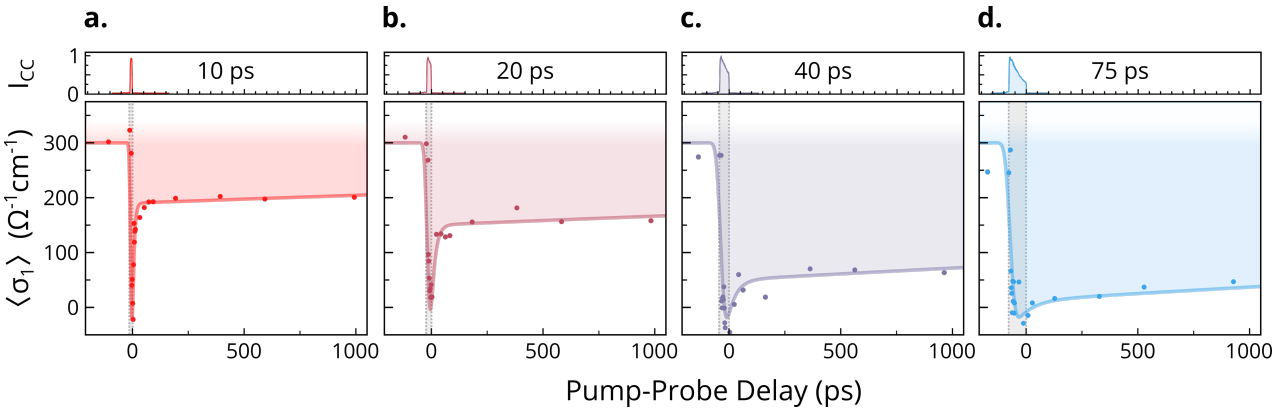

Figure S10.2: Time dependence of the real part of the optical conductivity $\sigma_1(\omega)$ averaged in the region of the photo-induced gap (2-10 meV). The subfigures show data for four different pulse lengths of **a.** 10 ps, **b.** 20 ps, **c.** 40 ps and **d.** 75 ps with respective excitation fluences of 12 mJ/cm^2, 18 mJ/cm^2, 46 mJ/cm^2 and 51 mJ/cm^2. These data were acquired at a base temperature T = 100 K. The top panels show the measured intensity time profile of the different excitation pulses.

S11 – Relaxation dynamics of the out-of-equilibrium metastable state

The relaxation dynamics of the metastable photo-induced superconducting state in K_3C_{60} were measured both optically and electronically. Figure S11a displays the time evolution of the photo-induced reduction of spectral weight in the real part of the optical conductivity $\Delta\sigma_1$ in the region between 2.2 meV and 10 meV. These measurements were performed on two different K_3C_{60} samples with a 10.6 μm pump pulse of 200 ps duration and at a fluence of 30 mJ/cm^2. The relaxation behavior can be modelled with an exponential decay with a time constant of ~12 ns (dashed line). To achieve optical delays longer than 2 ns we introduced additional fixed retardation lines into our setup to extend the range of the continuously tunable optical delay stages.

Figure S11b displays the time-dependent resistance of the laser irradiated K_3C_{60} pellet obtained from transient two-terminal measurements. The graph shows the same data presented in Fig. 4b. The inset, displays the time-dependence of the photo-induced resistance up to a time delay of 1 μs. The relaxation can be modelled with a double exponential decay (light blue solid line) one with a faster time constant τ_1~30 ns (compatible with what is shown in Figure S11a) and a second slower one with τ_2~550 ns.

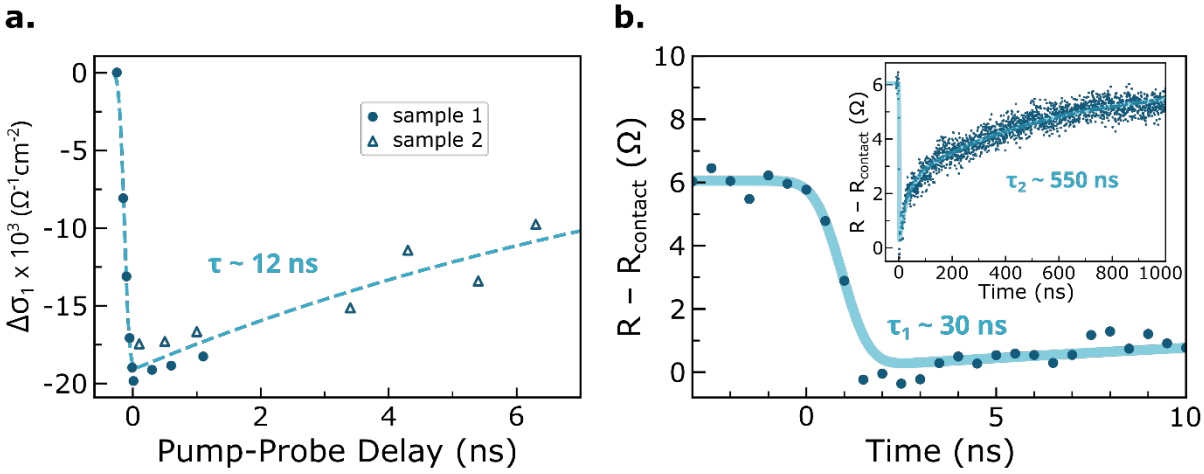

Figure S11: a. Time dependent spectral weight loss $\Delta\sigma_1$ as defined in supplementary section S8, measured on two different K_3C_{60} samples. The dashed line is a fit with a single exponential decay yielding a time constant τ_1~12 ns. **b.** Time-dependent resistance of a laser irradiated K_3C_{60} pellet obtained from high-frequency two-terminal transport measurements. The graph shows the same data as in Figure 4b. The inset displays the relaxation dynamics of the signal on a longer timescale. The light blue solid line is a fit with a double exponential decay function (τ_1~30 ns and τ_2~550 ns). All measurements were performed at an excitation wavelength of 10.6 μm, and base temperature T=100 K.

S12 – Temperature dependence of the out-of-equilibrium state

The temperature dependence of the out-of-equilibrium optical response of the photo-induced superconducting state in K_3C_{60} is shown in Figure S12. Therein, we report data measured at temperatures of 100 K, 200 K, and 300 K for increasing time delays of 10 ps, 100 ps, and 300 ps after photo-excitation with 1 ps long, 7.3 μm central wavelength pulses. The data acquired at 100K is also shown in Figure 2 of the main text.

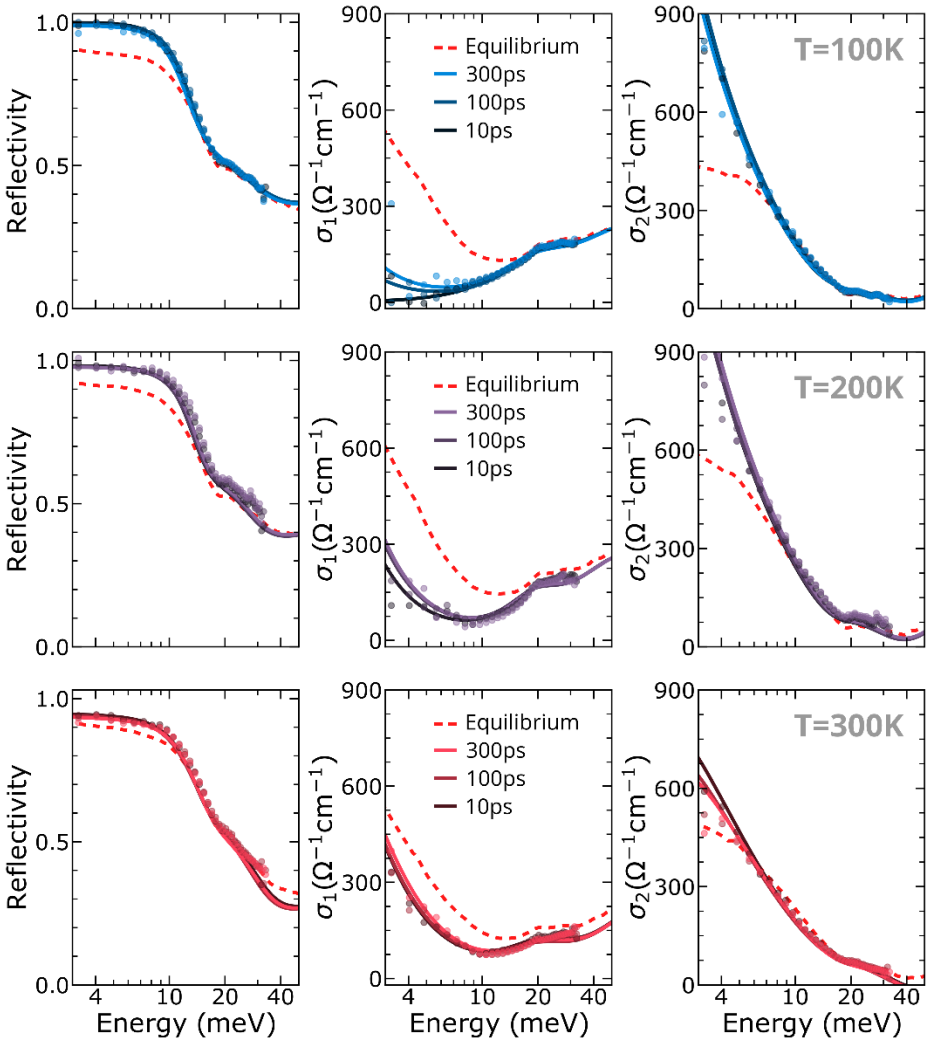

Figure S12: Temperature dependence of the light-induced optical properties. The measurements were performed at three different temperatures of 100 K, 200 K and 300 K (upper middle and lower row, respectively). Each row displays reflectivity (sample-diamond interface), real, and imaginary part of the optical conductivity measured at equilibrium (dashed lines), and 10, 100, and 300ps after photo-excitation (filled symbols). The solid lines are Drude-Lorentz fits to the transient optical data (cf. Supplementary Information S6). All measurements were performed using 1 ps long excitation pulses, centred at 7.3 μm wavelength, and with a fluence of 18 mJ/cm^2.

At temperatures above 100K, the light-induced gapping in $\sigma_1(\omega)$ is only partial and is significantly reduced as the temperature is increased. A similar behavior is also observed for the low-frequency divergence in $\sigma_2(\omega)$ that progressively vanishes upon heating. Interestingly, we note that for all measured temperatures the optical properties remained unchanged for 300 ps after excitation. This may suggest that precursors of the long-lived superconducting state discovered at 100 K are present all the way to room temperature.

S13 – Simulations of the superconducting order parameter relaxation

In the following, we describe a phenomenological theory for the relaxation of the superconducting order parameter following laser excitation. This model is similar to phenomenological models used for cuprate superconductors[16-18], shown to be capable to accurately reproduce a surprising amount of the available experimental data on these materials. As argued in the main text, in a situation where preformed pairs exist in the material above T_c, and superconductivity is destroyed by phase fluctuations, a laser-induced synchronized state can decay very slowly.

We considered a phenomenological Ginzburg-Landau model of the superconducting order parameter on a two-dimensional square lattice with 100x100 sites and periodic boundary conditions. The order parameter at site m is denoted $\psi_m(t) = |\psi_m| e^{i\,\phi_m}$, where $|\psi_m|$ is the local amplitude and ϕ_m the local phase. As in Ref. 16, we assumed that the order parameter is microscopically related to the local singlet pairs, i.e. $\psi_m \sim \langle\, c_{m\downarrow} c_{m\uparrow} - c_{m\uparrow} c_{m\downarrow} \,\rangle$, but no assumptions were made on how these pairs are generated microscopically.
The free energy potential was chosen as:

$$F = \sum_m (A\,|\psi_m|^2 + \frac{B}{2}|\psi_m|^4) + \frac{C}{2} \sum_{<m,n>} |\psi_m||\psi_n| \cos(\phi_n - \phi_m)\,,$$

where the summation $< m, n >$ runs over neighbouring sites. The first term describes a local potential which determines the equilibrium Cooper pair density. This theory contains three free parameters A, B, and C which we specify below. We chose the parameters such that the mean local order parameter is given by $\langle|\psi_m|\rangle = \sqrt{-A/B} = \sqrt{1 - T/T_0}$, where T_0 is the temperature at which Cooper pairs start to form in the material. The second term in the free energy potential couples adjacent sites and determines the phase stiffness. A positive parameter C means it is energetically favourable for the phases to align. The strength of this

phase coupling controls the temperature scale, at which the relative phase of pairs on different sites can lock and the condensate achieves phase coherence.

Here we focused on the situation where $C \ll |A|, B$, i.e. we consider a gas of localised bosons which weakly interact with one another. The weak interaction can lead to condensation only at low temperatures. Importantly, the model reproduces correctly the equilibrium phase transition at $\simeq$ 20 K as displayed in Figure S13.1.

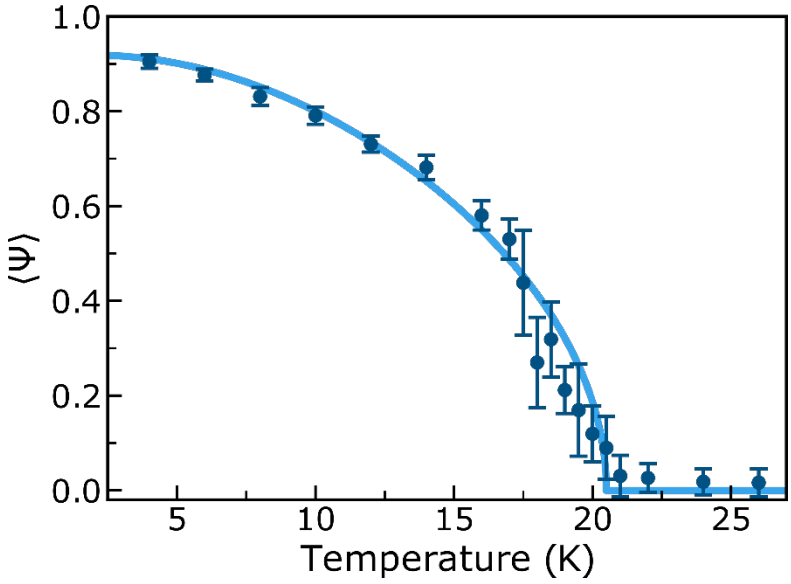

Figure S13.1: Temperature dependence of the amplitude of the average superconducting order parameter $\langle|\psi_m|\rangle$ calculated from the Ginzburg-Landau model described in the text, showing a transition at $T_c \simeq 20$ K. The light blue line is a guide to the eye.

To describe the nonequilibrium relaxation, we set the superconducting gap $2\Delta_0 \sim 10$ meV as observed in the transient optical measurements. To describe the relaxation of the photo-induced superconducting state we simulated the dynamics using the time-dependent Ginzburg-Landau (TDGL) equation:

$$\tau \partial_t \, \psi_m \, (t) = \, -\frac{\delta F(\psi_m, \psi_m^*)}{\delta \psi_m^*} + \eta_m(t),$$

where η_m(t) is a random force describing random thermal fluctuations and obeys $\langle \eta_m^*(t)\eta_{m'}(t')\rangle = 2\,\tau\,\frac{k_B T}{\mathrm{f}\,\Delta_0}\,\delta_{m,m'}\delta(t-t')$, where f is a dimensionless parameter which is introduced below. Here τ is a free parameter that determines the characteristic time scale at which the dynamics evolve and that needs to be determined from a fit to the experiments. We found that a good match between the measurements and simulated relaxation is obtained for $\tau \sim 1.5$ ps and f = 6000 (see figure 6 in the main text).

Discussion

If the order parameter is driven away from its equilibrium value, the time evolution due to the derivative of the free energy potential gives rise to an exponential decay back to its unperturbed value. For small perturbations, and neglecting the spatial variation of the order parameter, we linearize the TDGL equation as:

$$\tau \partial_t \psi_m(t) \simeq -|A| \psi_m(t),$$

to obtain the amplitude relaxation time

$$T_{amplitude} = \frac{\tau}{|A|}$$

This sets the time scale for relaxation driven by the deterministic part of the TDGL equation.

As our model considers a situation where incoherent Cooper pairs survive above the critical temperature, another relaxation time scale emerges naturally. It stems from the thermal diffusion of local phases taking place at the minimum $\sqrt{-A/B}$ of the local free energy potential. Below the critical temperature, the relative phases are kept fixed due to the coupling C. But above T_c, this attraction is overpowered by thermal noise and phase coherence is lost. To assess the timescale on which this should take place, we consider a high temperature regime where fluctuations dominate the dynamics,

$$\tau \partial_t \psi_m(t) \simeq \eta_m(t).$$

We consider the noise as $\eta_m = \eta_1 + i\,\eta_2$, where η_1 and η_2 are real-valued independent random variables, respectively. We note that $\langle \eta_1(t)\eta_1(t') \rangle = \langle \eta_2(t)\eta_2(t') \rangle = \tau \frac{k_B T}{f\,\Delta_0} \delta(t-t')$ and $\langle \eta_1 \eta_2 \rangle = 0$. Assuming that the amplitude has reached its equilibrium value $\langle |\psi_m| \rangle = \sqrt{1 - T/T_0}$, we obtain a time evolution equation for the phase:

$$\sqrt{1 - \frac{T}{T_0}}\, \tau\, \partial_t \phi_m(t) = \eta_2 \cos(\phi_m) - \eta_1 \sin(\phi_m) = \eta'(t).$$

In the second equality, we recognize that the noise term can again be written as a random noise η' with the same variance as η_1 and η_2. Consequently, we find that the phase undergoes a one-dimensional random walk induced by the random force η'. The diffusion time scale can be found by solving the associated Fokker-Planck equation for the probability distribution of ϕ_m (see e.g. Ref. 19). Solving this diffusion equation, we find the phase relaxation timescale:

$$T_{phase} = \frac{f\Delta_0(1 - T/T_0)}{\mathrm{k}_B T}\tau.$$

We note that in this case, it is determined by the ratio between the superconducting gap Δ_0 and the thermal energy $\mathrm{k}_B T$ of the environmental degrees of freedom.

The ratio between phase and amplitude relaxation time is proportional to the steepness of the free energy potential,

$$\frac{T_{phase}}{T_{amplitude}} \propto f.$$

If the free energy potential is shallow and amplitude fluctuations are large, the ratio can be close to one. If phase fluctuations dominate, phase relaxation becomes much slower than the amplitude relaxation. Furthermore, if the temperature of the environmental degrees of freedom in which the relaxation takes place, is close to the 'pseudogap' temperature T_0, the ratio becomes smaller. Fig. S13.2 displays snapshots of the phase distribution for different values of f. When $f = 60$, the potential is very shallow and the phases relax to a broad distribution with vanishing average amplitude. Clearly, in such a situation there can be no distinction between phase and amplitude relaxation. However, when f increases, amplitude fluctuations are suppressed and the local order parameters are confined to a narrow ring with

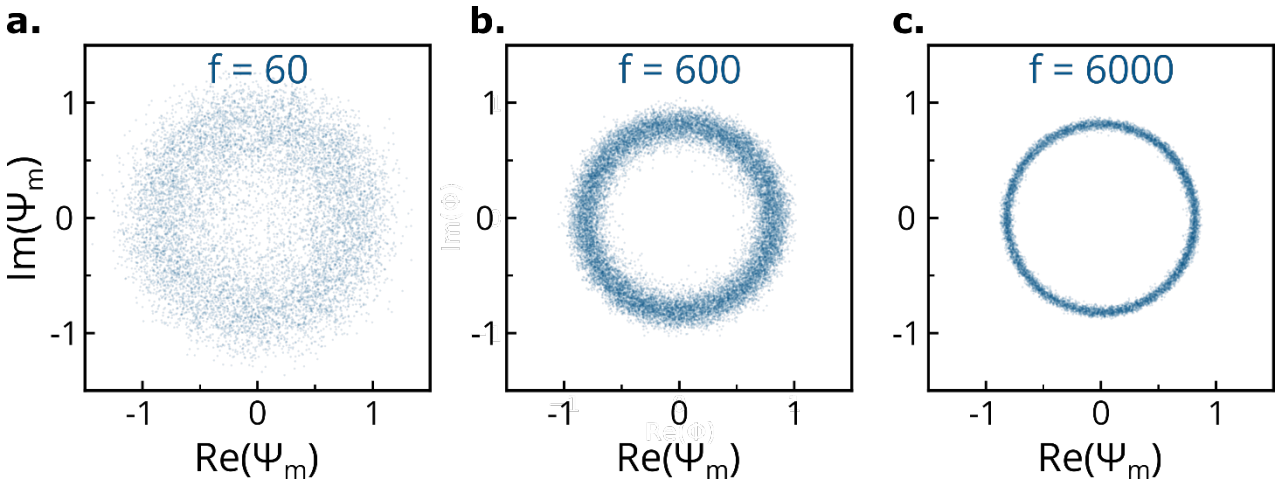

Figure S13.2: Snapshots of the on-site order parameter ψ_m in the complex plane after time evolution up to $t = 10^3 \frac{\tau}{|A|}$. The simulations were performed at $T = 100$ K using three different f parameter values of 60, 600, and 6000 (left to right). The on-site order parameters ψ_m are initialised in a synchronised state, $\psi_m(t = 0) = \sqrt{-A/B}$ and then relaxed according to the TDGL equation described in the text.

radius $\sqrt{-A/B}$. In such a situation, phase relaxation becomes the dominant relaxation pathway and a synchronised state can survive much longer.

Parametrization

We write the coefficients of the free energy as:

$$A = -\frac{\Delta_0}{k_B T_0}\left(1 - \frac{T}{T_0}\right)$$

$$B = \frac{\Delta_0}{k_B T_0},$$

$$C = -\frac{c}{f}\frac{\Delta_0}{k_B T_0},$$

where we assume that the relevant energy scale is $\Delta_0/k_B T_0$. Here we assume that A changes its sign at a very large temperature $T_0 = 300$ K, i.e. a local Cooper pair density can survive up to room temperature. In addition, we introduce the dimensionless parameter f, which determines the relative strength of amplitude fluctuations. This parameter determines the relative speed of the amplitude and phase relaxation: An increase of f reduces the absolute amplitude of thermal fluctuations as well as the pair coupling constant C, such that the superconducting transition temperature remains constant. Finally, the parameter $c = 4.5$ is adjusted to induce a superconducting transition at $\simeq 20$ K at equilibrium (see Figure S13.1).

References (Supplementary Material)

1 Cantaluppi, A. *et al.* Pressure tuning of light-induced superconductivity in K_3C_{60}. *Nature Physics* **14**, 837-841, (2018).

2 Mitrano, M. *et al.* Possible light-induced superconductivity in K_3C_{60} at high temperature. *Nature* **530**, 461-464, (2016).

3 Hebard, A. F. *et al.* Superconductivity at 18 K in potassium-doped C_{60}. *Nature* **350**, 600-601, (1991).

4 Degiorgi, L. *et al.* Optical properties of the alkali-metal-doped superconducting fullerenes: K_3C_{60} and Rb_3C_{60}. *Physical Review B* **49**, 7012-7025, (1994).

5 Degiorgi, L., Briceno, G., Fuhrer, M. S., Zettl, A. & Wachter, P. Optical measurements of the superconducting gap in single-crystal K_3C_{60} and Rb_3C_{60}. *Nature* **369**, 541-543, (1994).

6 Plaskett, J. S. & Schatz, P. N. On the Robinson and Price (Kramers—Kronig) Method of Interpreting Reflection Data Taken through a Transparent Window. *The Journal of Chemical Physics* **38**, 612-617, (1963).

7 Babzien, M., Pogorelsky, I. V. & Polanskiy, M. Solid-state seeding of a high power picosecond carbon dioxide laser. *AIP Conference Proceedings* **1777**, 110001, (2016).

8 Alcock, A. J. & Corkum, P. B. Ultra-Short Pulse Generation with CO_2 Lasers. *Philosophical Transactions of the Royal Society of London. Series A, Mathematical and Physical Sciences* **298**, 365-376, (1980).

9 Alcock, A. J., Corkum, P. B. & James, D. J. A fast scalable switching technique for high-power CO_2 laser radiation. *Appl. Phys. Lett.* **27**, 680-682, (1975).

10 Mayer, B. *et al.* Sub-cycle slicing of phase-locked and intense mid-infrared transients. *New Journal of Physics* **16**, 063033, (2014).

11 Kindt, J. T. & Schmuttenmaer, C. A. Theory for determination of the low-frequency time-dependent response function in liquids using time-resolved terahertz pulse spectroscopy. *The Journal of Chemical Physics* **110**, 8589-8596, (1999).

12 Schmuttenmaer, C. A. Exploring Dynamics in the Far-Infrared with Terahertz Spectroscopy. *Chemical Reviews* **104**, 1759-1780, (2004).

13 Born, M. & Wolf, E. *Principles of Optics*. 7th edn, (Cambridge University Press, 1999).

14 Nicoletti, D. *et al.* Optically induced superconductivity in striped $La_{2-x}Ba_xCuO_4$ by polarization-selective excitation in the near infrared. *Physical Review B* **90**, 100503, (2014).

15 Pozar, D. M. *Microwave Engineering*. 4th edn, 189-194 (Wiley, 2012).

16 Banerjee, S., Ramakrishnan, T. V. & Dasgupta, C. Phenomenological Ginzburg-Landau-like theory for superconductivity in the cuprates. *Physical Review B* **83**, 024510, (2011).

17 Sarkar, K., Banerjee, S., Mukerjee, S. & Ramakrishnan, T. V. The correlation between the Nernst effect and fluctuation diamagnetism in strongly fluctuating superconductors. *New Journal of Physics* **19**, 073009, (2017).

18 Sarkar, K., Banerjee, S., Mukerjee, S. & Ramakrishnan, T. V. Doping dependence of fluctuation diamagnetism in high T_c superconductors. *Annals of Physics* **365**, 7-23, (2016).

19 Bellac, M. L., Mortessagne, F. & Batrouni, G. G. *Equilibrium and non-equilibrium statistical thermodynamics*. (Cambridge University Press, 2004).